Bioactive Materials 6 (2021) 2105–2119

Contents lists available at ScienceDirect

Bioactive Materials

journal homepage: www.sciencedirect.com/journal/bioactive-materials

Immobilized thrombin on X-ray radiopaque polyvinyl alcohol/chitosan embolic microspheres for precise localization and topical blood coagulation

Xiaohong Li [a], Xiongfa Ji [b], Kun Chen [a], Muhammad Wajid Ullah [a], Basen Li [c], Jiameng Cao [a], Lin Xiao [d,**], Jun Xiao [e,***], Guang Yang [a,*]

[a] Department of Biomedical Engineering, College of Life Science and Technology, Huazhong University of Science and Technology, Wuhan, 430074, China
[b] Department of Orthopedics, Guangdong Provincial People's Hospital, Guangdong Academy of Medical Sciences, Guangzhou, 510080, China
[c] Department of Radiology, Tongji Hospital, Tongji Medical College, Huazhong University of Science and Technology, Wuhan, 430030, China
[d] School of Biomedical Engineering, Sun Yat-sen University, Guangzhou, 510006, China
[e] Department of Orthopaedics, Tongji Hospital, Tongji Medical College, Huazhong University of Science and Technology, Wuhan, 430030, China

ARTICLE INFO

Keywords:
$BaSO_4$
Polyvinyl alcohol/chitosan
Radiopacity
Thrombin
Coagulation
Embolization

ABSTRACT

Trans-catheter arterial embolization (TAE) plays an important role in treating various diseases. The available embolic agents lack X-ray visibility and do not prevent the reflux phenomenon, thus hindering their application for TAE therapy. Herein, we aim to develop a multifunctional embolic agent that combines the X-ray radiopacity with local procoagulant activity. The barium sulfate nanoparticles ($BaSO_4$ NPs) were synthesized and loaded into the polyvinyl alcohol/chitosan (PVA/CS) to prepare the radiopaque $BaSO_4$/PVA/CS microspheres (MS). Thereafter, thrombin was immobilized onto the $BaSO_4$/PVA/CS MS to obtain the thrombin@$BaSO_4$/PVA/CS MS. The prepared $BaSO_4$/PVA/CS MS were highly spherical with diameters ranging from 100 to 300 μm. *In vitro* CT imaging showed increased X-ray visibility of $BaSO_4$/PVA/CS MS with the increased content of $BaSO_4$ NPs in the PVA/CS MS. The biocompatibility assessments demonstrated that the MS were non-cytotoxic and possessed permissible hemolysis rate. The biofunctionalized thrombin@$BaSO_4$/PVA/CS MS showed improved hemostatic capacity and facilitated hemostasis *in vitro*. Additionally, *in vivo* study performed on a rabbit ear embolization model confirmed the excellent X-ray radiopaque stability of the $BaSO_4$/PVA/CS MS. Moreover, both the $BaSO_4$/PVA/CS and thrombin@$BaSO_4$/PVA/CS MS achieved superior embolization effects with progressive ischemic necrosis on the ear tissue and induced prominent ultrastructural changes in the endothelial cells. The findings of this study suggest that the developed MS could act as a radiopaque and hemostatic embolic agent to improve the embolization efficiency.

1. Introduction

Minimally invasive procedures to treat a variety of cancerous and noncancerous diseases, such as unresectable hepatocellular carcinoma [1], benign prostatic hyperplasia [2], uterine fibroids [3], and acute hemorrhage [4], have gained much attention in the clinic. Particularly, *trans*-catheter arterial embolization (TAE) is generally considered safe and effective in interventional therapy, which selectively delivers the embolic agents to the target artery under X–ray guidance. It exerts therapeutic effects by deliberately blocking the blood vessel, thereby cutting off the nutrition and oxygen supply to the target tissue or organ. The characteristics of embolic agents play an important role in the performance of TAE treatment [5,6]. Over the past few years, there have been growing concerns with the radiolucent nature of the embolic agents [7,8]. This issue can be addressed to some extent by physically mixing the embolic agent with iodinated contrast medium (e.g., iohexol) and delivering the mixture to the target arteries [9,10]. However, the main disadvantages of this method include several aspects. First, the contrast medium is easily dissociated from the embolic agent and results in fuzzy imaging and misdiagnosis [11]. Second, the rapid diffusion of

Peer review under responsibility of KeAi Communications Co., Ltd.
* Corresponding author.
** Corresponding author.
*** Corresponding author.
E-mail addresses: xiaolin23@mail.sysu.edu.cn (L. Xiao), jun_xiao@hust.edu.cn (J. Xiao), gyang-hust@hust.edu.cn (G. Yang).

https://doi.org/10.1016/j.bioactmat.2020.12.013
Received 2 August 2020; Received in revised form 16 December 2020; Accepted 16 December 2020

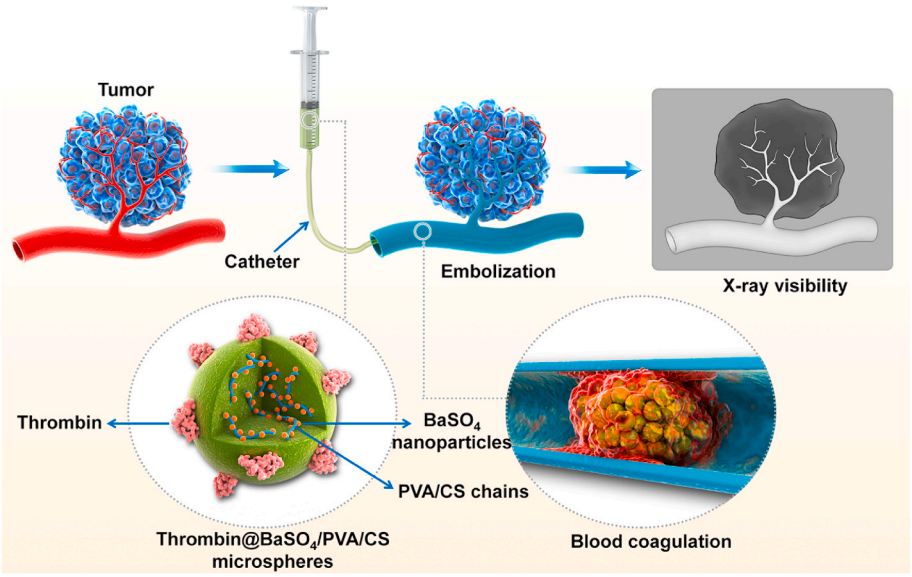

Scheme 1. Schematic illustration of the thrombin@$BaSO_4$/PVA/CS MS as an embolic agent that combines X-ray visibility and local blood coagulation.

the contrast medium causes difficulties in re-examination after TAE [12]. Third, the iodinated contrast medium may cause adverse events in some patients who suffer from thyroid disorder [13]. Besides, there are some other strategies to achieve precise visualization of the embolic agents. For example, the copolymerization method is always employed to prepare the iodine-containing polymeric embolic agents [14,15]; however, the preparation process is complicated, and the iodinated polymers exhibit potential toxicity [16]. Alternatively, the radiopacity of the embolic microspheres (MS) could be achieved by encapsulating heavy metal salts in the polymeric MS [17,18]. Barium sulfate ($BaSO_4$) has been used as a contrast agent for gastrointestinal examination due to its high X-ray attenuation, biocompatibility, cost-effectiveness, and insolubility [19,20]. However, the commercially available $BaSO_4$ particles are in the micro-scale size, and show inferior performance of radiographic contrast compared to the nano-sized $BaSO_4$ particles [21,22]. Therefore, it is crucial to synthesize $BaSO_4$ nanoparticles (NPs) and load them within the embolic agent, which could provide a radiopaque formulation suitable for clinical use in TAE.

Another challenge associated with the embolization process is the reflux phenomenon in some cases [23,24]. This phenomenon can potentially result in significant complications, including the non-target embolization, catheter entrapment, and even treatment failure [25–27]. Triggered by these complications, two strategies have been proposed to avoid the reflux effect. One option is to use a balloon catheter for controlling the reflux during the embolization. However, there exists the risk of vessel damage caused by the balloon inflation, catheter entrapment, catheter fracturing, and the increased concomitant intranidal pressure and associated bleeding [28–30]. The other option is to pause the injection for a while in the case of reflux until the embolic particles penetrate more distally into the vasculature. Nonetheless, this procedure is mainly limited to liquid embolic agents and undoubtedly increases the operation complexity and fluoroscopy time [29,31].

Thrombin, a serine protease with procoagulant activity, accelerates the conversion of fibrinogen to fibrin and promotes the rapid formation of thrombus and hemostasis [32,33]. Considering the intrinsic hemostatic properties of thrombin, it is of vital importance to develop a biofunctionalized embolic agent *via* covalently binding thrombin onto the embolic agent to cause adequate hemostatic effects, and prevent the reflux effect.

In recent years, polyvinyl alcohol (PVA) has been extensively used in many biomedical fields due to its excellent biocompatibility, non-immunogenicity, as well as good chemical and thermal stability [34,35]. Specifically, the PVA MS are commercially available in the clinic and regarded as a permanent embolic agent [6,36]. Although PVA MS have been successfully used for treating various diseases, there exist several limitations associated with them, most notably, the lack of X-ray radiopacity and inability to prevent the reflux phenomenon. Such limitations restrict their use and development in TAE applications.

Herein, we developed thrombin-immobilized and $BaSO_4$-loaded embolic MS, which combined the X-ray visibility and local blood coagulation activities. The developed MS were used for precise localization and avoidance of the reflux effect during the embolization procedure (Scheme 1). More specifically, $BaSO_4$ NPs were first synthesized and characterized, followed by adding to PVA/CS polymeric matrix with varied contents to prepare the $BaSO_4$-loaded PVA/CS ($BaSO_4$/PVA/CS) MS *via* inverse suspension crosslinking method. The addition of a small content of CS in the composite MS was beneficial to obtain the well-dispersed MS, where it was positively charged in acidic conditions and acted as a barrier to prevent the aggregation of MS. The prepared $BaSO_4$/PVA/CS MS were comprehensively characterized for their physicochemical properties, X-ray visibility, cytocompatibility, and hemocompatibility. Thereafter, biofunctionalization of $BaSO_4$/PVA/CS MS was performed *via* covalent binding of thrombin on their surface and further evaluated their procoagulant activity. Moreover, *in vivo* X-ray radiopacity and embolization efficacy were investigated in a rabbit central auricular artery model.

2. Materials and methods

2.1. Materials

Poly (vinyl alcohol) 124 (PVA-124, Mw~105 kDa, degree of hydrolysis 98.0–99.8 mol%), barium chloride ($BaCl_2$), and ammonium sulfate ($(NH_4)_2SO_4$) were obtained from Sinopharm Chemical Reagent Co., Ltd. (Shanghai, China). Thrombin and chitosan (CS, Mw = 110–150 kDa, 93% degree of deacetylation) were provided by Sigma-Aldrich (Beijing, China). Glutaraldehyde (GA, 50 wt%) and 4-dimethylaminopyridine (DMAP) were received from Macklin Biochemical Co., Ltd. (Shanghai, China). Succinic anhydrate, 2-[4-(2-hydroxyethyl)piperazin-1-yl]ethanesulfonic acid (HEPES), 1-(3-Dimethylaminopropyl)-3-ethylcarbodiimide hydrochloride (EDC), and *N*-hydroxysuccinimide (NHS) were obtained from Aladdin Reagent Co., Ltd. (Shanghai, China). Fetal bovine serum (FBS), DMEM medium, and antibiotics (penicillin: 100 IU/mL + streptomycin: 100 mg/mL) were provided by Gibco Life

Technology Co., Ltd. (Grand Island, USA). CCK-8 assay kit was produced by Dojindo Laboratories (Kumamoto, Japan).

In vivo animal tests were performed on New Zealand white rabbits supplied by the Experimental Animal Center in our institution, and the experiments were complied with the guidelines established by the Institutional Animal Care and Use Committee.

2.2. Preparation of $BaSO_4$/PVA/CS MS

The $BaSO_4$ NPs were prepared by a precipitation method *via* the reaction between $BaCl_2$ and $(NH_4)_2SO_4$ aqueous solutions at appropriate concentrations (See details in the Supporting Information). The prepared $BaSO_4$ NPs were loaded inside the PVA/CS MS through the solid-in-water-oil (S/W/O) emulsification crosslinking method according to a previous report with some modifications [37]. Briefly, 8.6% (w/v) PVA solution was prepared by dissolving PVA powder in hot water at 80 °C. Similarly, CS was dissolved in 1 wt% acetic acid solution to form a 0.84% (w/v) CS solution. The PVA and CS solutions were mixed and stirred to form a homogeneous blend solution (CS:PVA = 1:19, w/w). The $BaSO_4$ NPs-containing PVA/CS solution was prepared at 10, 20, and 30 wt% loading by mixing the required contents of $BaSO_4$ NPs with PVA/CS solution, and subjected to high-speed homogenization. The obtained suspension was then added dropwise into the n-heptane containing 2.8% (w/v) Span 80 with continuous stirring at 480 rpm. After 30 min, a mixture of GA (2.6 mL, 25 wt%) and diethyl ether (DEE, 4.15 mL) was added to PVA/CS solution at a volume ratio of 0.03:1, and continued stirring for 5 min. Afterwards, a small volume of 1 M HCl (catalyst) was added to facilitate the crosslinking process. The reaction was carried out at 55 °C for 5 h. After cooling to room temperature, the resultant $BaSO_4$/PVA/CS MS were recovered from n-heptane by centrifugation, and rinsed with petroleum ether, followed by rinsing with ethanol for several times, and finally rinsed thoroughly with distilled water. Thereafter, the $BaSO_4$/PVA/CS MS were immersed in 4 wt% glycine aqueous solution for 12 h to remove the excess of unreacted GA and vacuum-dried. Similarly, the PVA/CS MS were also prepared following the above protocol except the addition of $BaSO_4$ NPs. Finally, all prepared MS were sieved to the final size of 100–300 μm.

2.3. Immobilization of thrombin on $BaSO_4$/PVA/CS MS

Considering the syringeability and X-ray detectability, 20 wt% $BaSO_4$/PVA/CS MS were selected and used in the following experiments. The carboxylated $BaSO_4$/PVA/CS MS were used to immobilize the thrombin. The detailed modification procedure of $BaSO_4$/PVA/CS MS is provided in the Supporting Information. The succinylated $BaSO_4$/PVA/CS MS were suspended in 100 mM EDC and 25 mM NHS in anhydrous dimethyl sulfoxide (DMSO) and gently stirred at 25 °C for 1 h. Then, the MS were thoroughly rinsed with DMSO to remove the unreacted EDC and NHS. Subsequently, the thrombin solution was prepared by dissolving 1 mg of thrombin (1000 U/mg) in HEPES buffer (20 mM, 0.15 M NaCl, pH 8.2), and then added to the above activated MS. After incubation at room temperature for 1.5 h, the resultant thrombin-immobilized $BaSO_4$/PVA/CS (thrombin@$BaSO_4$/PVA/CS) MS were extensively rinsed with HEPES buffer, freeze-dried, and stored at −20 °C for further use. In the immobilization experiment, the $BaSO_4$/PVA/CS MS were used as the control.

2.4. Characterization

The surface and cross-sections of the MS were observed under a field emission scanning electron microscope (FESEM). The elemental analysis of $BaSO_4$ NPs, PVA/CS, and $BaSO_4$@PVA/CS MS was carried out by energy dispersive X-ray (EDX). A field emission transmission electron microscope (FETEM) was used to study the morphology of the synthesized $BaSO_4$ NPs. The size distribution of $BaSO_4$ NPs was determined from different FETEM images. The chemical compositions of $BaSO_4$ NPs, PVA/CS, and $BaSO_4$@PVA/CS MS were determined by Fourier transform infrared (FTIR) spectrometer. The crystalline state of $BaSO_4$ NPs loaded into the $BaSO_4$@PVA/CS MS was determined by an X-ray diffractometer (XRD). Thermogravimetric analysis (TGA) was performed at a heating rate of 10 °C/min. The immobilization of thrombin on the surface of $BaSO_4$@PVA/CS MS was determined through X-ray photoelectron spectra (XPS, Kratos Axis Ultra DLD, Japan) analysis. The X-ray radiopacity test of the MS was performed on a 128-row CT scanner. The images were recorded and then transferred to an external workstation for further analysis. The characterization details are provided in the Supporting Information.

2.5. In vitro biocompatibility studies

The viability of HVSMCs incubated with $BaSO_4$/PVA/CS MS was quantitatively evaluated by CCK-8 assay based on the indirect contact model. Briefly, the MS were sterilized with Co^{60} radiation for 12 h (9 kGy), and then 10 and 20 mg/mL MS were immersed in DMEM containing 10% FBS and 1% antibiotics, and incubated at 37 °C for 24 h to obtain the cell culture extracts. The positive control was prepared by using the cell culture medium containing 0.64% phenol as recommended by ISO10993-5 [38], while the culture medium was used as the negative control. The HVSMCs at a density of 5×10^3 cells/well were seeded in 96-well plates and incubated under 5% CO_2, 37 °C, and 95% humidity for 24 h prior to use. The MS extracts and controls were added to the 96-well plates. At predetermined time points (24, 48, and 72 h), the cell viability was quantified *via* CCK-8 assay. The relative cell viability was calculated relative to the negative control group. All experiments were repeated six times. The cell viability was further evaluated by Live/Dead cell assay, while the cell morphology on the MS was observed under FESEM. The detailed experimental procedures are provided in the Supporting Information.

The hemolysis potential of $BaSO_4$/PVA/CS MS was evaluated similar to that described by Wang et al. [39]. Briefly, the fresh whole blood was obtained from a New Zealand white rabbit *via* a marginal ear vein puncture, and collected in medical vacuum tubes containing acid citrate dextrose (ACD) as an anticoagulant (ACD:blood = 1:9, v/v). Thereafter, 10 and 20 mg/mL disinfected MS were separately immersed in tubes filled with 1 mL of normal saline at 37 °C for 1 h. Afterwards, 20 μL of diluted blood (4 mL of fresh blood + 5 mL of normal saline) was added to the MS and incubated at 37 °C for another 1 h. The positive and negative controls were prepared by adding 20 μL of diluted blood in 1 mL of distilled water and saline solution, respectively. After incubation, all samples were centrifuged, and the absorbance of supernatants was measured at 545 nm by a UV–Vis spectrophotometer. The percentage of hemolysis was calculated according to equation (1).

$$\text{Hemolysis}(\%) = \frac{OD\ test - OD\ neg}{OD\ pos - OD\ neg} \times 100 \quad (1)$$

where OD_{test}, OD_{pos}, and OD_{neg} are the absorbance of the test samples, positive control, and negative control, respectively. Each experiment was performed in triplicate.

2.6. In vitro hemostatic performance study

The whole blood clotting kinetics tests were performed according to a previously reported method with some modifications [40]. Briefly, the anticoagulant whole blood was re-calcified by adding 100 μL of 0.1 M $CaCl_2$ to 1 mL of fresh whole blood. Subsequently, 200 μL of activated blood was immediately added to each tube containing 10 mg of MS and incubated at 37 °C for different time intervals of 5, 20, 35, and 50 min. At each time point, 6 mL of distilled water was added to each tube and maintained at 37 °C for 5 min to lyse the red blood cells (RBCs), which were not trapped in the blood clots. The RBCs were hemolyzed, and the absorbance of the resultant hemoglobin solution was measured at 545

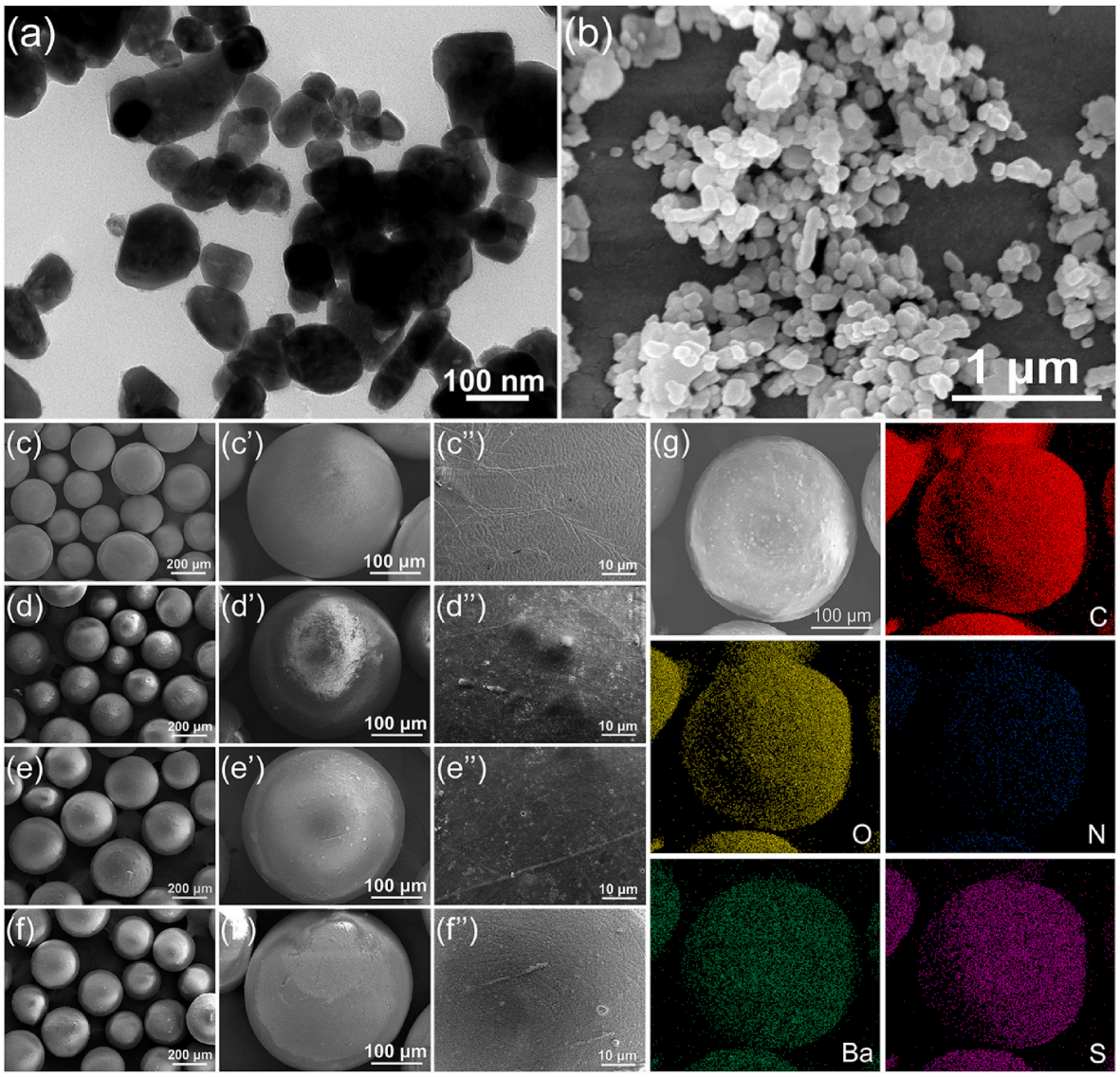

Fig. 1. FETEM (a) and FESEM (b) images of as-prepared $BaSO_4$ NPs, and FESEM surface morphology of (c-c'') PVA/CS MS, (d-d'') 10 wt% $BaSO_4$/PVA/CS MS, (e-e'') 20 wt% $BaSO_4$/PVA/CS MS, and (f-f'') 30 wt% $BaSO_4$/PVA/CS MS, respectively. (g) Is the EDX mapping images of a single 20 wt% $BaSO_4$/PVA/CS MS.

nm with a UV–Vis spectrophotometer. The blood sample without mixing with MS was used as an experimental control and tested following the same protocol. Five replicates were run for each sample.

The hemostatic properties of thrombin@$BaSO_4$/PVA/CS MS were further investigated in terms of the adhesion of whole blood and RBCs on MS, as well as the MS-induced fibrin formation. The anticoagulant whole blood was centrifuged at 250 g for 15 min and the precipitated RBCs were collected for RBCs adhesion assay. The RBCs were added to the MS in a 24-well plate and incubated at 37 °C for 1 h. After that, the MS were rinsed twice with saline solution, and then suspended in 2.5 wt% GA to fix the RBCs for 1 h. The MS-RBCs constructs were subjected to sequential dehydration with gradually ascending concentrations of ethanol (30%, 50%, 70%, 80%, 90%, 95%, and 100%), and then freeze-dried. Similar to the RBCs adhesion assay, the whole blood was incubated with the samples at 37 °C for 1 h. After that, the samples were fixed, dehydrated, and freeze-dried. To evaluate the fibrin formation induced by the MS, the platelet-rich plasma (PRP) was collected by centrifuging the whole blood at 250 g for 15 min, and the concentration of the blood platelets was quantified to be 1,506,040 ± 320,500/μL using a hemocytometer. Subsequently, the obtained PRP was re-calcified by adding 0.1 M $CaCl_2$ at a volume ratio of 9:1. The MS were incubated with re-calcified PRP in a 24-well plate at 37 °C for 5 min. Thereafter, the samples were fixed in 2.5 wt% GA and allowed to dry in lyophilizer. All samples were vacuum-coated with gold for 300 s prior to FESEM observation.

2.7. *In vivo* embolization studies

2.7.1. *In vivo* rabbit ear artery embolization and X-ray visibility tests

The rabbits (2.5 ± 0.5 kg, male) were anesthetized by administering 30 mg/kg pentobarbital sodium from the marginal ear vein. Afterwards, the rabbit ear hair was shaved, and the ears were disinfected with 75% ethanol. Then, an incision was made on the ear skin to identify the central auricular artery. Thereafter, PVA/CS, $BaSO_4$@PVA/CS, and thrombin@$BaSO_4$/PVA/CS MS at a concentration of 20 mg/mL were mixed with glycerol, and then infused slowly using a 22-Gauge puncturing needle. The rabbits treated with glycerol alone were designated as the control. After that, the injection site was pressed until it stopped bleeding. The changes in the color and shape of the embolized ears were inspected at 0, 7, 15 days, and recorded by photography. The X-ray visible stability test was performed *in vivo* after embolization with PVA/CS and $BaSO_4$@PVA/CS MS for 3, 7, and 15 days. The rabbits were

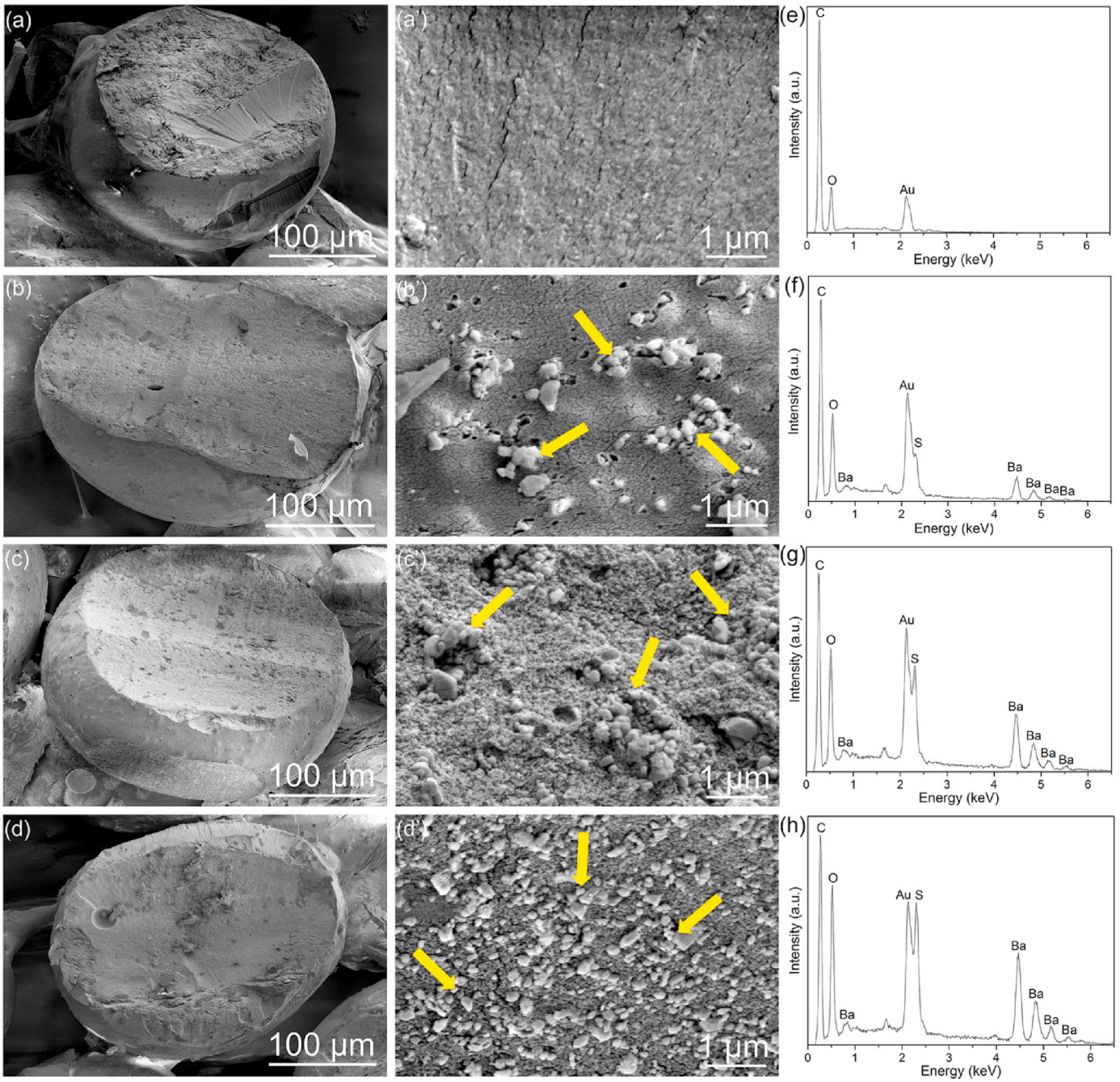

Fig. 2. FESEM images of the cross-sectional morphologies of (a, a') PVA/CS MS, (b, b') 10 wt% $BaSO_4$/PVA/CS MS, (c, c') 20 wt% $BaSO_4$/PVA/CS MS, and (d, d') 30 wt% $BaSO_4$/PVA/CS MS, respectively. (e)–(h) are the corresponding EDX spectra of the cross-sections of PVA/CS and 10, 20, and 30 wt% $BaSO_4$/PVA/CS MS. The yellow arrows indicate the presence of $BaSO_4$ NPs in the cross-sectional structures of the MS.

subjected to X-ray imaging using an X-ray machine (General Electric, XR/A, 80 keV, exposure time 0.2 s). All images were obtained from the same animal, and the *in vivo* X-ray radiopacity of each sample was compared.

2.7.2. Histopathological examination and ultrastructural findings

At 7 and 15 days post-embolization, the rabbits were sacrificed, and the infarcted tissues containing embolic MS were resected and fixed in 4% paraformaldehyde for 48 h prior to evaluation by histopathological analysis. Thereafter, the central auricular artery and the surrounding tissue were dissected, embedded in paraffin, and then cut into 5 μm thick cross-sections. The sections were further stained with hematoxylin-eosin (H&E) and Masson's trichrome, and examined under an optical microscope. After 15 days, the morphological and ultrastructural changes in the vascular endothelial cells in different treated groups were investigated *via* FETEM. The details are presented in the Supporting Information.

2.8. Statistical analysis

The results obtained were analyzed by student's *t*-test (SPSS 20.0, IBM, Armonk, USA). The difference between groups was statistically significant at $P < 0.05$, and $P < 0.01$ indicated an extraordinary significant difference.

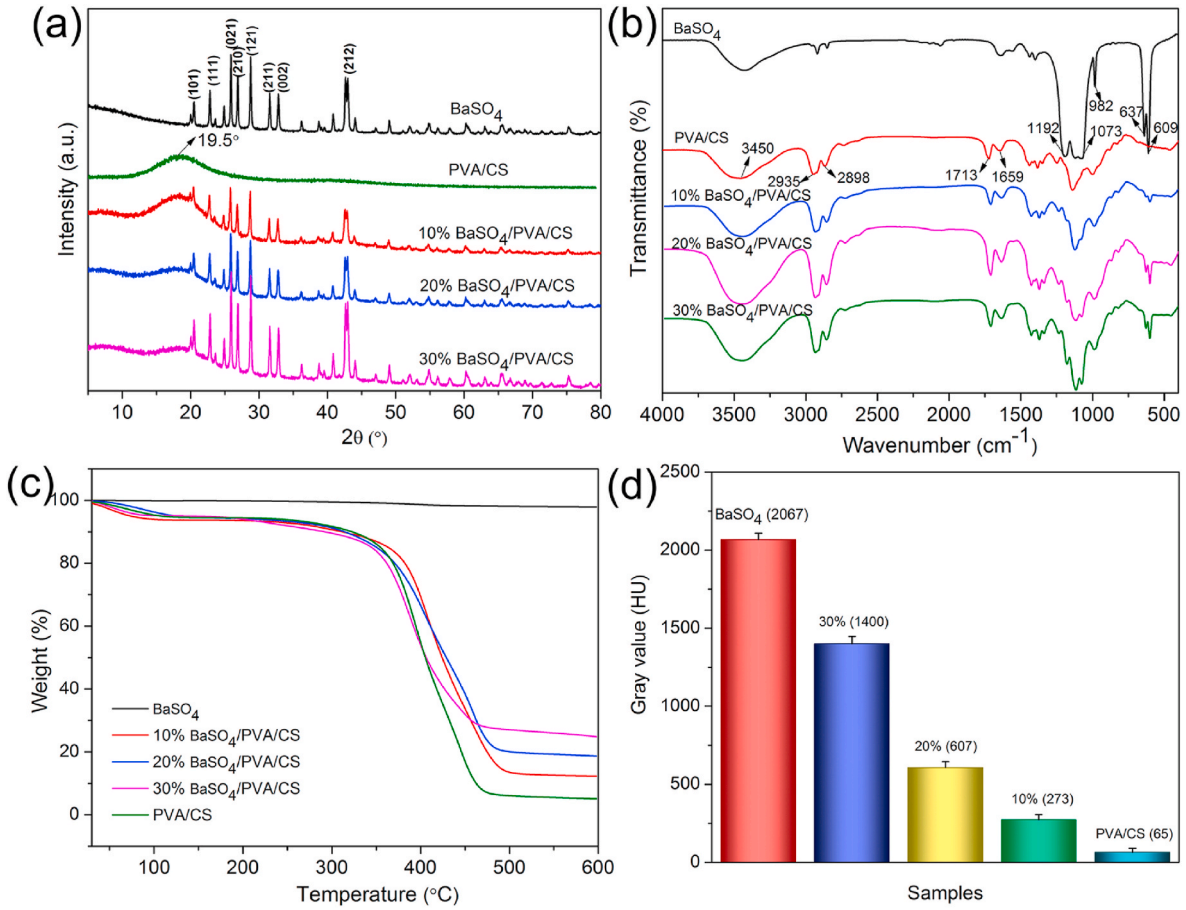

Fig. 3. Characterization of $BaSO_4$/PVA/CS MS. (a) XRD patterns, (b) FTIR spectra, and (c) TGA curves of $BaSO_4$ NPs, PVA/CS, and 10, 20, 30 wt% $BaSO_4$/PVA/CS MS, and (d) show the radiopacity values of the samples (n = 3).

3. Results and discussion

3.1. Microstructure examination of $BaSO_4$/PVA/CS MS

The typical FETEM image of as-synthesized $BaSO_4$ NPs is presented in Fig. 1a. It is evident that the particles are nano-sized, and exhibit an elliptical-shaped structure with a smooth surface, which is further verified by the FESEM observation (Fig. 1b). The size distribution of the $BaSO_4$ NPs is presented in Fig. S1a, which shows that the mean particle size is 81.7 ± 20.4 nm. EDX analysis of $BaSO_4$ NPs revealed the compositional distribution of Ba and S elements among the nanocrystals. Besides, a small content of C element was also detected, which could possibly be derived from the resin stub (Fig. S1b).

The surface morphologies of PVA/CS MS with and without the loading of $BaSO_4$ NPs were observed by FESEM. As shown in Fig. 1c-c'', the blank PVA/CS MS are well-dispersed and possess a perfectly spherical shape with a smooth surface. After loading of various contents of $BaSO_4$ NPs, the $BaSO_4$/PVA/CS composite MS exhibited no difference with regard to the dispersity and morphological characteristics as compared to the blank MS (Fig. 1d-f''). It should be noted that, upon loading of the $BaSO_4$ NPs with different contents into the PVA/CS MS, all the $BaSO_4$/PVA/CS MS maintained their smooth surface without superfluous $BaSO_4$ NPs on the MS surface, indicating ideal miscibility between $BaSO_4$ NPs and PVA/CS matrix. The similarity in the shape and surface features of these MS is consistent with the trends that reported in previous studies [41,42]. In addition, the dense layer of $BaSO_4$/PVA/CS MS was supposed to prevent the $BaSO_4$ NPs from leaking out and to maintain a long time radiopacity *in vivo*. This can be explained by the fact that the chemical covalent crosslinking of PVA/CS polymeric matrix with GA improved the strength of $BaSO_4$/PVA/CS MS. Moreover, the obtained MS were 100–300 μm in diameter, which was an appropriate size for embolizing the central auricular artery of rabbits. The EDX elemental mapping analysis was further carried out for 20 wt% $BaSO_4$/PVA/CS MS to study the $BaSO_4$ NPs distribution in the composite MS. As shown in Fig. 1g, the Ba and S elements were found to be homogeneously distributed throughout the MS, indicating that the $BaSO_4$ NPs were dispersed well in the interior of the PVA/CS matrix.

To study the internal structure of the composite MS and the miscibility of $BaSO_4$ NPs within the PVA/CS polymeric matrix, the cross-sections of pure PVA/CS and $BaSO_4$/PVA/CS MS with 10, 20, and 30 wt% $BaSO_4$ NPs loading were observed under FESEM. The cross-sectional view shows that the $BaSO_4$ NPs are entrapped in the dense PVA/CS polymeric matrix (Fig. 2b-d'), unlike the rough texture for pure PVA/CS polymer (Fig. 2a,a'). It is worth noting that, in the higher magnification images, the $BaSO_4$ NPs showed a tendency to form separate domains and exhibited compacted clusters throughout the MS (indicated by yellow arrows). More importantly, with the increased contents of $BaSO_4$ NPs in the PVA/CS MS, the composite MS were formed with the loading of more $BaSO_4$ NPs in a single MS. To further verify the loading of $BaSO_4$ NPs inside the PVA/CS polymeric matrix, EDX analysis was carried out to determine the elemental compositions on the cross-sections of PVA/CS and $BaSO_4$/PVA/CS MS containing different contents of $BaSO_4$ NPs (Fig. 2e–h). Fig. 2e shows the presence of C and O elements, which are derived from the PVA/CS MS. In addition, the Au element was also detected, which came from the sputtered gold layer. The EDX spectra of $BaSO_4$/PVA/CS MS showed the presence of other elements such as Ba and S were also detected as compared to the PVA/CS MS. This indirectly verified that the $BaSO_4$ NPs were

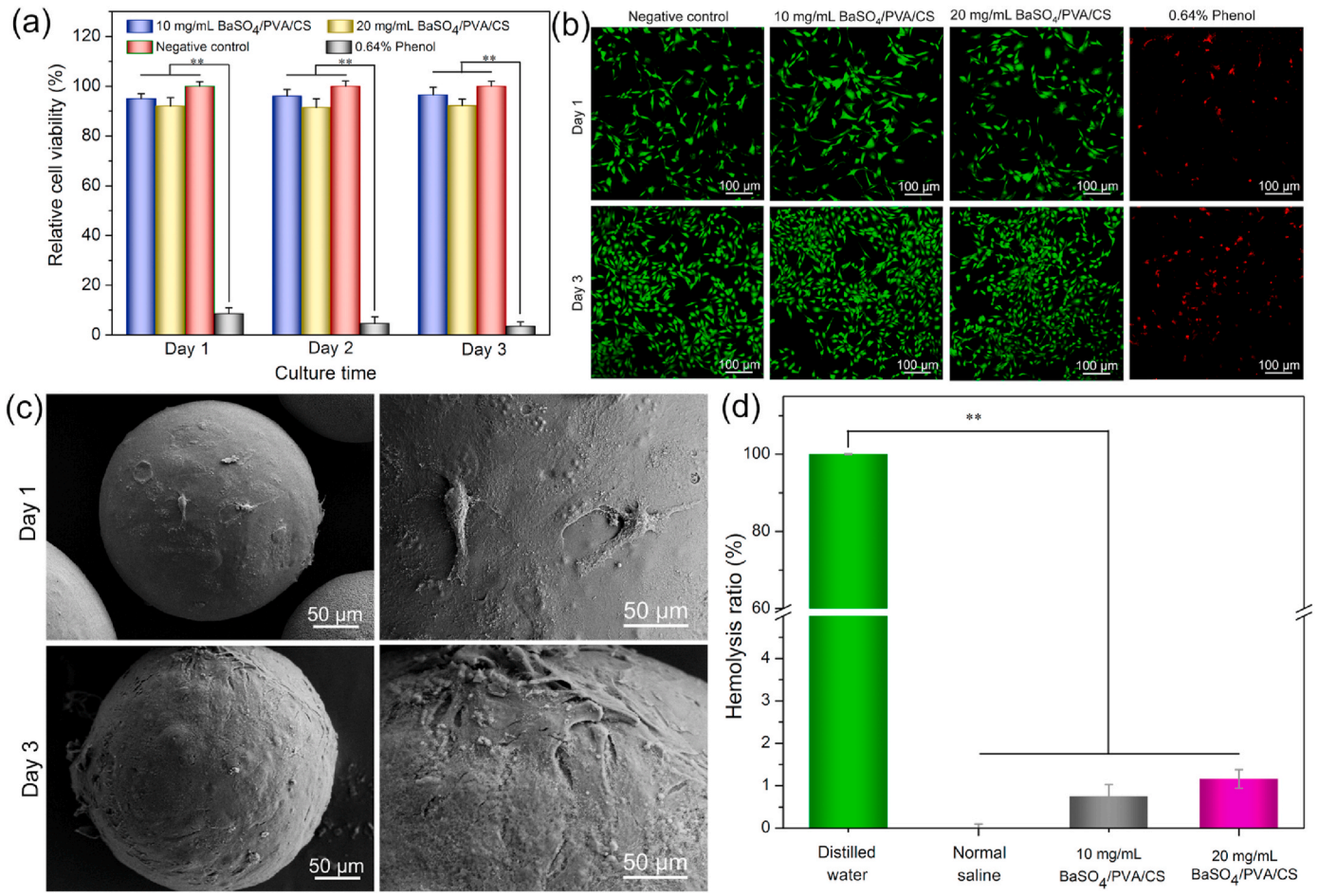

Fig. 4. *In vitro* biocompatibility evaluation of $BaSO_4$/PVA/CS MS. (a) *In vitro* cell viability of HVSMCs incubated with $BaSO_4$/PVA/CS MS extracts at various concentrations for a different time period, $^{**}P < 0.05$ indicates a statistically significant difference with respect to the positive control group (n = 6). (b) CLSM images of HVSMCs after incubation in the control and experimental groups for 1 and 3 days. (c) FESEM observations of HVSMCs on the surface of $BaSO_4$/PVA/CS MS after incubation for 1 and 3 days. (d) Hemolysis ratios of diluted rabbit blood after incubation with 10 and 20 mg/mL $BaSO_4$/PVA/CS MS at 37 °C for 1 h. The blood incubated with distilled water was taken as 100% hemolyzed, while that incubated with normal saline was taken as 0% hemolyzed, respectively.

successfully loaded into the PVA/CS MS. Moreover, the intensity of characteristic peaks of Ba and S elements increased with the increased content of $BaSO_4$ NPs in the PVA/CS MS. Thus, it could be speculated that the X-ray radiopacity of the MS would be increased with the increase of $BaSO_4$ NPs, which was favorable for their application as a radiopaque embolic agent for further use *in vivo*.

3.2. Characterization and X-ray visibility of $BaSO_4$/PVA/CS MS

3.2.1. XRD analysis

The XRD patterns of pure $BaSO_4$ NPs, blank PVA/CS, and $BaSO_4$/PVA/CS MS are presented in Fig. 3a. The XRD pattern of $BaSO_4$ NPs showed that all diffraction peaks are in accordance with the barite structure (JCPDS card No. 24–1035). Particularly, the diffraction peaks at 20.4°, 22.8°, 25.8°, 26.8°, 28.7°, 31.5°, 32.8°, and 42.9° could be indexed as typical (101), (111), (021), (210), (121), (211), (002), and (212) planes of $BaSO_4$ crystals, respectively. This result confirms that the resultant NPs are pure $BaSO_4$ with an orthorhombic barite crystal structure. The XRD pattern of PVA/CS MS shows the broad peak appearing at around 19.5°, which can be attributed to the semi-crystalline structure. In the case of $BaSO_4$ NPs loaded formulations with various contents, the sharp peaks associated with the crystalline state were evident, which could be attributed to the presence of $BaSO_4$ NPs in the PVA/CS MS. In addition, the intensity of the characteristic peaks increased with the increased content of $BaSO_4$ NPs in the PVA/CS MS. Moreover, the characteristic peaks remained distinguishable, indicating that $BaSO_4$ NPs exhibited phase stability during the loading process, which suggests their suitability for embolization applications.

3.2.2. FTIR analysis

FTIR analysis was carried out to investigate the loading of $BaSO_4$ NPs into the PVA/CS MS. As depicted in Fig. 3b, the FTIR spectrum of $BaSO_4$ NPs reveals that the broad absorption bands at 1073–1192 and 982 cm^{-1}, which were attributed to the symmetrical vibrations of SO_4^{2-}. The absorption bands at 609 and 637 cm^{-1} were assigned to the out-of-plane bending vibration of SO_4^{2-}. For PVA/CS MS, a wide absorption band at around 3450 cm^{-1} was associated with the –OH stretching vibrations. The intense bands at 2898 and 2935 cm^{-1} were associated with the characteristic $–CH_2$-.symmetric and asymmetric stretching vibrations. Besides, the characteristic absorption bands at 1713 and 1659 cm^{-1} were assigned to C═O and C═C stretching vibrations, respectively. The FTIR spectrum for CS did not exist in the composite MS, which might be due to the insensitivity of the instrument to detect a small content of CS in the MS. Noticeably, the relative intensity of the characteristic bands derived from $BaSO_4$ NPs could be clearly seen in the spectra of $BaSO_4$/PVA/CS MS, and increased with the increased content of $BaSO_4$ NPs in the PVA/CS MS, which further confirms the successful loading of $BaSO_4$ NPs into the PVA/CS MS.

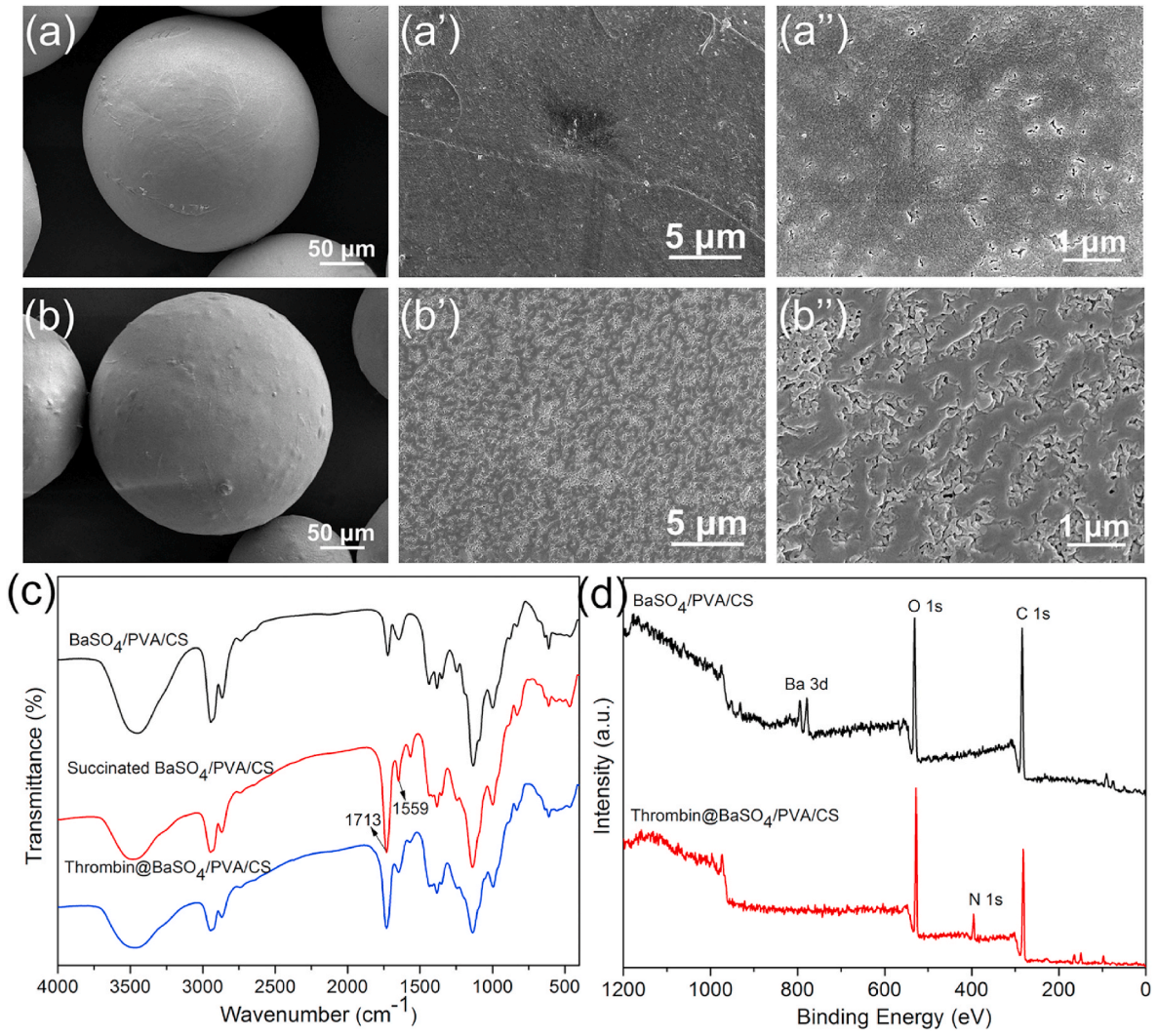

Fig. 5. FESEM surface morphology of (a-a'') $BaSO_4$/PVA/CS MS and (b-b'') thrombin@$BaSO_4$/PVA/CS MS. (c) FTIR spectra of $BaSO_4$/PVA/CS, succinated $BaSO_4$/PVA/CS, and thrombin@$BaSO_4$/PVA/CS MS. (d) XPS spectra of $BaSO_4$/PVA/CS and thrombin@$BaSO_4$/PVA/CS MS.

3.2.3. TGA

The exact content of $BaSO_4$ NPs in the MS as well as their thermal behavior were analyzed by TGA. As shown in Fig. 3c, the $BaSO_4$ NPs showed negligible weight loss when the sample was heated from 30 to 600 °C, indicating their excellent thermal stability. The TGA thermograms of PVA/CS and $BaSO_4$/PVA/CS MS with different $BaSO_4$ contents showed similar weight loss behavior, where two phases of weight loss were observed. The initial weight loss between 30 and 200 °C was ascribed to the evaporation of physically adsorbed water, while the sharp weight loss between 200 and 500 °C was attributed to the decomposition of the polymer. Beyond 500 °C, there was no considerable weight changes in the TGA curves. The final weight loss of PVA/CS MS and 10, 20, and 30 wt% $BaSO_4$/PVA/CS MS were 94.8%, 87.5%, 81.3%, and 74.8%, respectively. These results reveal that the thermal stability of $BaSO_4$/PVA/CS MS was increased with the increased content of $BaSO_4$ NPs. In addition, the actual contents of $BaSO_4$ NPs in 10, 20, and 30 wt% $BaSO_4$/PVA/CS MS were calculated to be 7.3%, 13.5%, and 20.0%, respectively, compared to the PVA/CS MS. Hence, the $BaSO_4$ NPs content in the MS matrix indicated a relatively high level, which would ensure an excellent X-ray detectability of the prepared MS.

3.2.4. In vitro X-ray visibility study

The X-ray imaging was performed to verify the X-ray visibility performance of $BaSO_4$/PVA/CS MS. Fig. S2 shows that the X-ray visibility increased gradually with the increased content of $BaSO_4$ NPs in the PVA/CS MS. Furthermore, the quantitative radiopacity evaluation indicated that the 10 wt% $BaSO_4$/PVA/CS MS showed a mean radiopacity of 273 Hounsfield Unit (HU) and increased to 607 and 1400 HU when the $BaSO_4$ NPs content increased to 20 wt% and 30 wt%, respectively ($n = 5$) (Fig. 3d). Thus, the $BaSO_4$/PVA/CS MS with a suitable content of $BaSO_4$ NPs could act as an effective radiopaque embolic agent, which was traceable under X-ray irradiation.

3.3. In vitro biocompatibility evaluations of $BaSO_4$/PVA/CS MS

3.3.1. Cytocompatibility examination

Considering the fact that the MS to be used as embolic materials should be safe and non-toxic [43], it is therefore important to determine their cytocompatibility. The viability of HVSMCs co-cultured with the extracts of MS for 24, 48, and 72 h was determined using CCK-8 assay (Fig. 4a). The cells co-cultured with 10 and 20 mg/mL extracts of $BaSO_4$/PVA/CS MS showed a relative cell viability of 95.0% and 92.0% on day 1, 96.0% and 91.5% on day 2, and reached about 96.5% and 92.2% on day 3, respectively. No significant difference was observed between the MS and negative control group throughout the incubation period ($P > 0.05$), suggesting no cytotoxic effects of the MS towards the HVSMCs. In contrast, the relative cell viability decreased as a function of time, and all values were lower than 10% when in contact with the

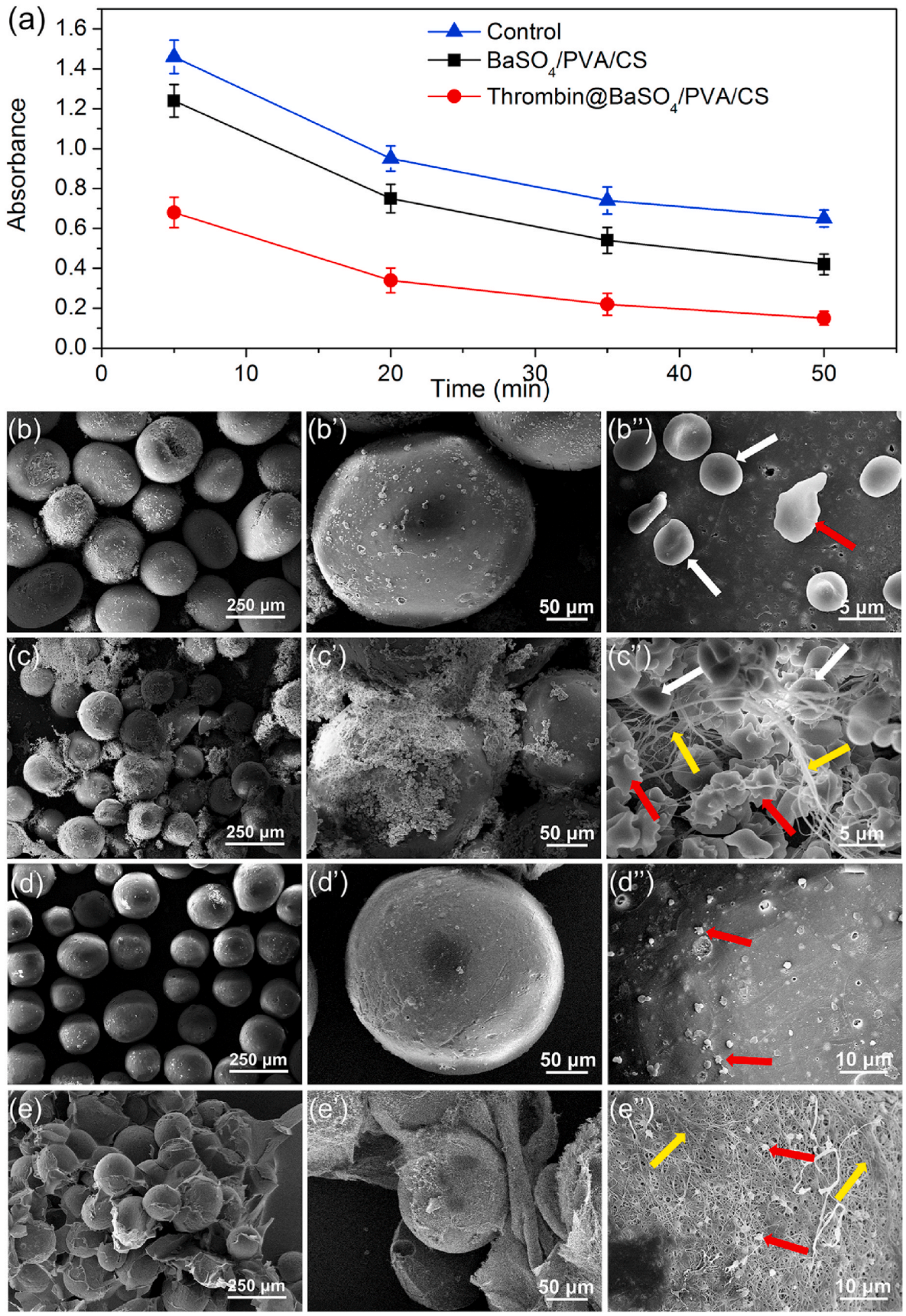

Fig. 6. (a) Whole blood clotting kinetics of the control (blood without MS), $BaSO_4$/PVA/CS, and thrombin@$BaSO_4$/PVA/CS MS. FESEM images of whole blood clotting on the surface of (b-b'') $BaSO_4$/PVA/CS and (c-c'') thrombin@$BaSO_4$/PVA/CS MS; fibrin network formed on the surface of (d-d'') $BaSO_4$/PVA/CS and (e-e'') thrombin@$BaSO_4$/PVA/CS MS (White arrow: RBCs; Red arrow: platelets; Yellow arrow: fibrin).

0.64% phenol containing medium (positive control). This indicated that the cell viability of the positive control was significantly lower than that of the MS and negative control group ($P < 0.01$). These results suggest that the MS extracts were able to preserve the cell viability and, thus, have no cytotoxicity. In this study, the presence of residual GA released from the MS might be a concern regarding the cytotoxicity. It is reported that the cytotoxicity may occur at a high concentration of GA [44]. The GA-crosslinked MS were rinsed thoroughly with distilled water, and further treated with 4 wt% glycine solution to react with the aldehyde groups in the residual GA [45]; thus, the potential toxicity was greatly minimized. With regard to the appropriate concentrations of MS in the cytotoxicity studies, most researchers performed the cytotoxicity analysis at a concentration of 10 or 20 mg/mL of the MS [46–49]. A previous report by Campos et al. showed that when increased the concentrations of GA-crosslinked chitosan–PVA microparticles (CCPMS) to 10.0% (v/v), there was no significant difference in the cell viability compared to the 2.0% (v/v) MS [50]. Accordingly, in our experiment, the viability of HVSMCs might decrease slightly but not significantly if the concentration of the MS increased to 30 or 40 mg/mL. The MS may still retain the excellent cytocompatibility at these concentrations. On the other hand, the maximum concentration of MS was maintained at 20 mg/mL in order to maintain the consistency with the following animal tests.

The viability of HVSMCs incubated with 10 and 20 mg/mL MS, the medium (negative control), and 0.64% phenol containing medium (positive control) were determined *via* Live/Dead cell assay. As illustrated in Fig. 4b, the cells showed good attachment and normal growth morphology, with predominantly alive cells (stained green) and almost no dead red spots (dead cells) both on the negative control and MS group on day 1. After three days, the cells had grown and spread uniformly and extensively, and distributed more densely in the negative control and MS groups. In addition, the cell numbers in the MS groups were comparable to the negative control, indicating that the MS were non-cytotoxic and biocompatible. However, in the positive control group, massive dead cells (stained red) were observed both on day 1 and day 3, which could be due to the cytotoxic effect of phenol towards the cells. These observations were consistent with the CCK-8 assay results (Fig. 4a).

The characteristic cell morphology of HVSMCs on the surface of $BaSO_4$/PVA/CS MS was further investigated *via* FESEM. As shown in Fig. 4c, after incubation for one day, it was observed that the MS supported the cell adhesion and growth, where the cells tended to spread and maintained physical contact with each other through the filopodia. On day 3, the cells proliferated further and stretched to form confluent monolayers on the MS surface.

Overall, the results of cytocompatibility analysis imply that the MS are nontoxic towards the HVSMCs, and could be safe for *in vivo* embolization.

3.3.2. *In vitro hemolysis analysis*

One of the critical prerequisites of the embolic agents to be used in contact with the blood should not induce hemolysis upon implantation [51,52]. Thus, the hemolysis behavior of the $BaSO_4$/PVA/CS MS was evaluated by incubating the MS with fresh rabbit blood. As represented in Fig. 4d, the hemolysis ratios of $BaSO_4$/PVA/CS MS at the concentration of 10 and 20 mg/mL were 0.75% and 1.16%, respectively, which was significantly lower than that of the positive control ($p < 0.01$). Generally, the hemolysis ratio of less than 5% is considered as an acceptable value [53], thus, the hemolysis results indicate the non-hemolytic nature of $BaSO_4$/PVA/CS MS. The hemolysis photograph further confirm that the $BaSO_4$/PVA/CS MS were hemocompatible (Fig. S3).

3.4. *Characterization of thrombin@$BaSO_4$/PVA/CS MS*

The comparative FESEM morphology studies between the free and thrombin-immobilized $BaSO_4$/PVA/CS MS with different magnifications are shown in Fig. 5a-b''. Apparently, both the $BaSO_4$/PVA/CS MS without or with thrombin display a similar spherical morphology. The surface features of $BaSO_4$/PVA/CS MS before thrombin immobilization indicate their relatively compact and smooth surface (Fig. 5a-a''). Contrarily, the MS immobilized with thrombin indicate that the coverage of thrombin occurred on the MS surface (Fig. 5b-b''). The magnified FESEM images show that the thrombin@-$BaSO_4$/PVA/CS MS possessed a relatively rough layer with enzyme evenly distributed, as compared to the smooth surface of $BaSO_4$/PVA/CS MS. These morphological features confirm the immobilization of thrombin on the MS surface.

The carboxylation of $BaSO_4$/PVA/CS MS and immobilization of thrombin onto the carboxylated $BaSO_4$/PVA/CS MS were confirmed through ATR-FTIR analysis. As represented in Fig. 5c, the FTIR spectrum of $BaSO_4$/PVA/CS MS showed that both the characteristic absorption peaks of $BaSO_4$ and PVA/CS. After carboxylation with succinic anhydride, it is clear that the grafted $BaSO_4$/PVA/CS MS showed an increased peak intensity at 1713 cm^{-1} and introduced a new peak at 1559 cm^{-1}, both of which were derived from the carbonyl groups that were formed during the ring-opening of the anhydride on the MS surface [54]. After the biofunctionalization of the grafted $BaSO_4$/PVA/CS MS with thrombin, there was no appreciable peak change compared to the grafted $BaSO_4$/PVA/CS MS, except the decreased peak intensity at 1713 and 1559 cm^{-1}. This result might be due to the reaction between the carbonyl groups on the grafted $BaSO_4$/PVA/CS MS and the amide groups on the thrombin, which decreased the number of carbonyl groups on the MS surface. On the other hand, the peak for –CO–NH-groups did not appear in the FTIR spectra, which could be due to the insensitivity of ATR-FTIR to detect the thin layer of thrombin.

The introduction of thrombin on the surface of $BaSO_4$/PVA/CS MS was further verified by XPS analysis. Fig. 5d presents the XPS spectra of $BaSO_4$/PVA/CS and thrombin@$BaSO_4$/PVA/CS MS. The most significant difference between the spectra is the N1s at 398 eV, and could be due to the presence of thrombin after the surface biofunctionalization. The quantitative evaluation results of XPS demonstrated that the mass ratio of N atoms in the thrombin@$BaSO_4$/PVA/CS MS was 8.6%, which indirectly reflected the content of thrombin immobilized on the MS surface. Thus, the XPS data provided additional evidence for the introduction of thrombin after the surface modification. The peaks for Ba centered at 777 and 793 eV were not presented in the spectrum of thrombin@$BaSO_4$/PVA/CS MS, which might account for the coverage of thrombin minimize the Ba signal. All these results confirm the successful immobilization of thrombin on the carboxylated $BaSO_4$/PVA/CS MS, which would enable fast local coagulation of blood following embolization.

3.5. *Hemolytic properties of thrombin@$BaSO_4$/PVA/CS MS*

3.5.1. *Whole blood clotting kinetics*

To evaluate the effectiveness of thrombin@$BaSO_4$/PVA/CS MS on activation of blood coagulation, the whole blood clotting kinetics as a function of time was conducted *in vitro*. In view of the main component of the blood clot was RBCs, the absorbance values of the blood are inversely proportional to the hemostatic efficiency of the materials assessed [55]. Fig. 6a shows the whole blood clotting kinetics of control, $BaSO_4$/PVA/CS, and thrombin@$BaSO_4$/PVA/CS MS. It is clear that at 5 min, the thrombin@$BaSO_4$/PVA/CS MS show significantly lower absorbance values than the $BaSO_4$/PVA/CS MS, suggesting that the thrombin@$BaSO_4$/PVA/CS MS induced a rapid blood clotting. In the following time points measured from 20 to 50 min, the absorbance values of both the groups showed a similar tendency to decrease, indicating that the blood clots were gradually formed on the MS surface. Moreover, in the serial time point, the thrombin@$BaSO_4$/PVA/CS MS exhibited a significantly faster whole blood clotting rate as compared to the $BaSO_4$/PVA/CS MS. These results demonstrate that the $BaSO_4$/PVA/CS MS with immobilized thrombin would lead to the enhanced

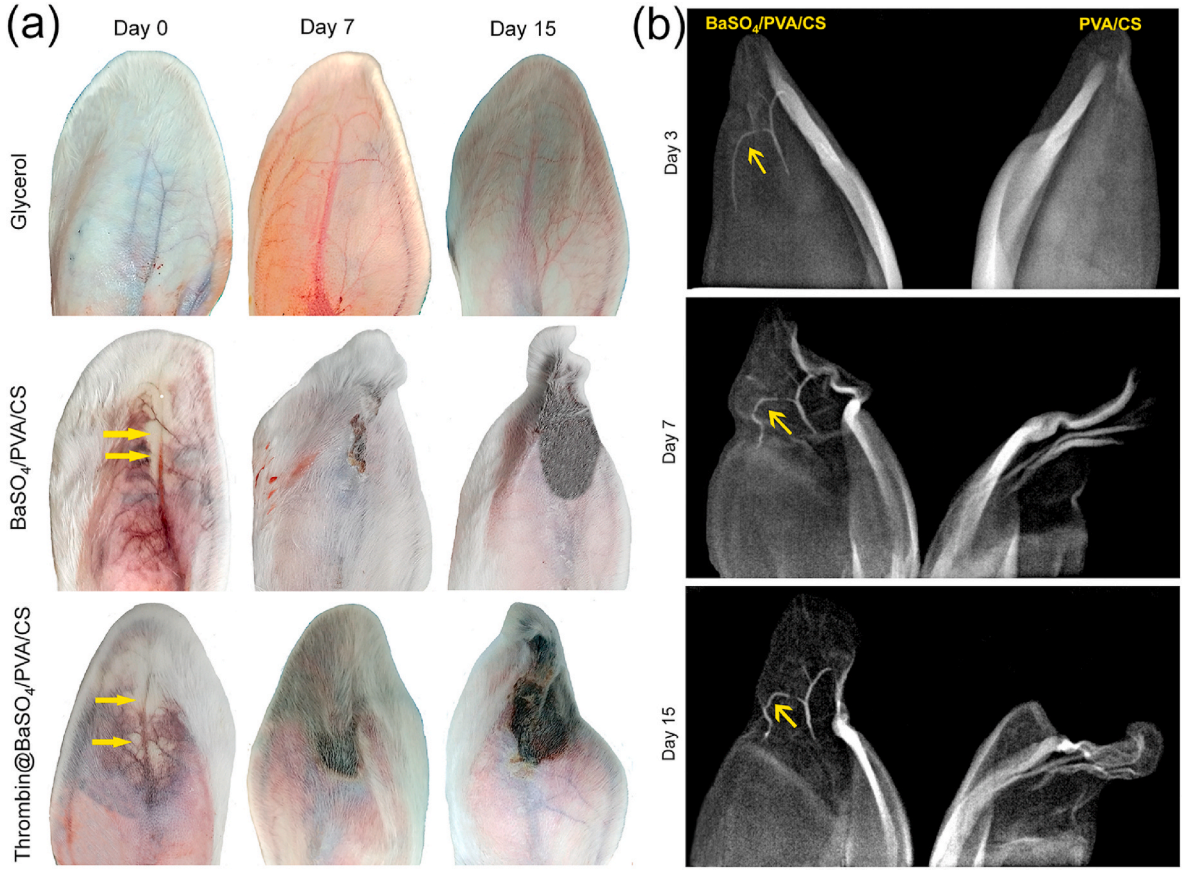

Fig. 7. (a) The gross observations of rabbit ear necrotic changes after treatment with glycerol, $BaSO_4$/PVA/CS, and thrombin@$BaSO_4$/PVA/CS MS for 0, 7, and 15 days. The yellow arrows indicate that the blood flow was interrupted and the vessel occlusion was achieved. (b) The X-ray images of rabbit ears treated with PVA/CS and $BaSO_4$/PVA/CS MS at predetermined time intervals (3, 7, and 15 days). The yellow arrows show the distribution of radiopaque MS within the central auricular arteries and side branches.

hemostatic efficiency. Compared to the control group, the $BaSO_4$/PVA/CS MS group showed a faster whole blood clotting rate, which could be due to the intrinsic physicochemical properties of the MS. On one hand, the polymeric $BaSO_4$/PVA/CS MS absorbed water from the blood and swelled, and led to the concentration and adhesion of RBCs on the MS, followed by initiation of blood clotting. On the other hand, the presence of a small content of CS in the $BaSO_4$/PVA/CS MS endowed them with a positively charged surface, which absorbed more RBCs (negatively charged) electrostatically and accelerated the blood clotting [56,57]. Fig. S4 shows that the blood gelled in contact with the thrombin@$BaSO_4$/PVA/CS MS for 100 s, while the blood still retained flowability in the presence of $BaSO_4$/PVA/CS MS, suggesting that the thrombin@$BaSO_4$/PVA/CS MS could effectively promote the blood coagulation.

3.5.2. Adherence of whole blood, RBCs, and fibrin on MS

The whole blood coagulation upon incubation with the thrombin@$BaSO_4$/PVA/CS MS was examined *via* FESEM. As shown in Fig. 6c-c'', it is observed that the thrombin@$BaSO_4$/PVA/CS MS were aggregated with blood clots. More specifically, the fibrin network covered the MS surface, with RBCs and deformed platelets entrapped. This is due to that the thrombin immobilized on the MS surface led to the activation of the intrinsic blood coagulation cascade [58]. Compared to the thrombin@$BaSO_4$/PVA/CS MS, the $BaSO_4$/PVA/CS MS demonstrated a lower hemostatic activity with respect to few RBCs and platelets captured on their surface (Fig. 6b-b''). It is therefore believed that the $BaSO_4$/PVA/CS MS immobilized with thrombin showed better blood clot formation. Similarly, the thrombin@$BaSO_4$/PVA/CS MS enhanced the RBCs adhesion on the surface compared to the $BaSO_4$/PVA/CS MS (Fig. S5).

As the immobilized thrombin acted as a coagulant by stimulating the conversion of fibrinogen into fibrin, the fibrin formation on the MS was investigated after incubation with the PRP. As shown in Fig. 6e-e'', the fibrin network combined with the platelets was formed on the surface of thrombin@$BaSO_4$/PVA/CS MS, forming a clot to entrap the MS. In contrast, the $BaSO_4$/PVA/CS MS did not show a fibrin network on their surface, the MS were well dispersed with few adhered platelets (Fig. 6d-d''). These results indicate that the thrombin@$BaSO_4$/PVA/CS MS possessed excellent hemostatic activities and, could be a potential hemostatic embolic agent.

3.6. In vivo embolization performance

3.6.1. Macroscopic observations of vessel embolization

The embolization behavior and efficacy of $BaSO_4$/PVA/CS MS were inspected by macrography. The results are shown in Fig. 7a. It is evident that there were no abnormalities in those injected with glycerol in the whole course. It was likely that the glycerol solution flew into the branches without blocking the ear arteries. Therefore, the rabbit ears treated with glycerol did not show ischemic necrosis or related complications. Conversely, as indicated by the arrows, the ears immediately became pale along the arterial course upon injection with $BaSO_4$/PVA/CS or thrombin@$BaSO_4$/PVA/CS MS, which was attributed to that the vascular occlusion effectively prevented the blood flow into the posterior arteries. After embolization for 7 days, a small area of blackened skin necrosis was observed, suggesting that the injection of MS was sufficient to impede the blood flow at the injection site and induced the tissue ischemic necrosis after a certain period of embolization. On day

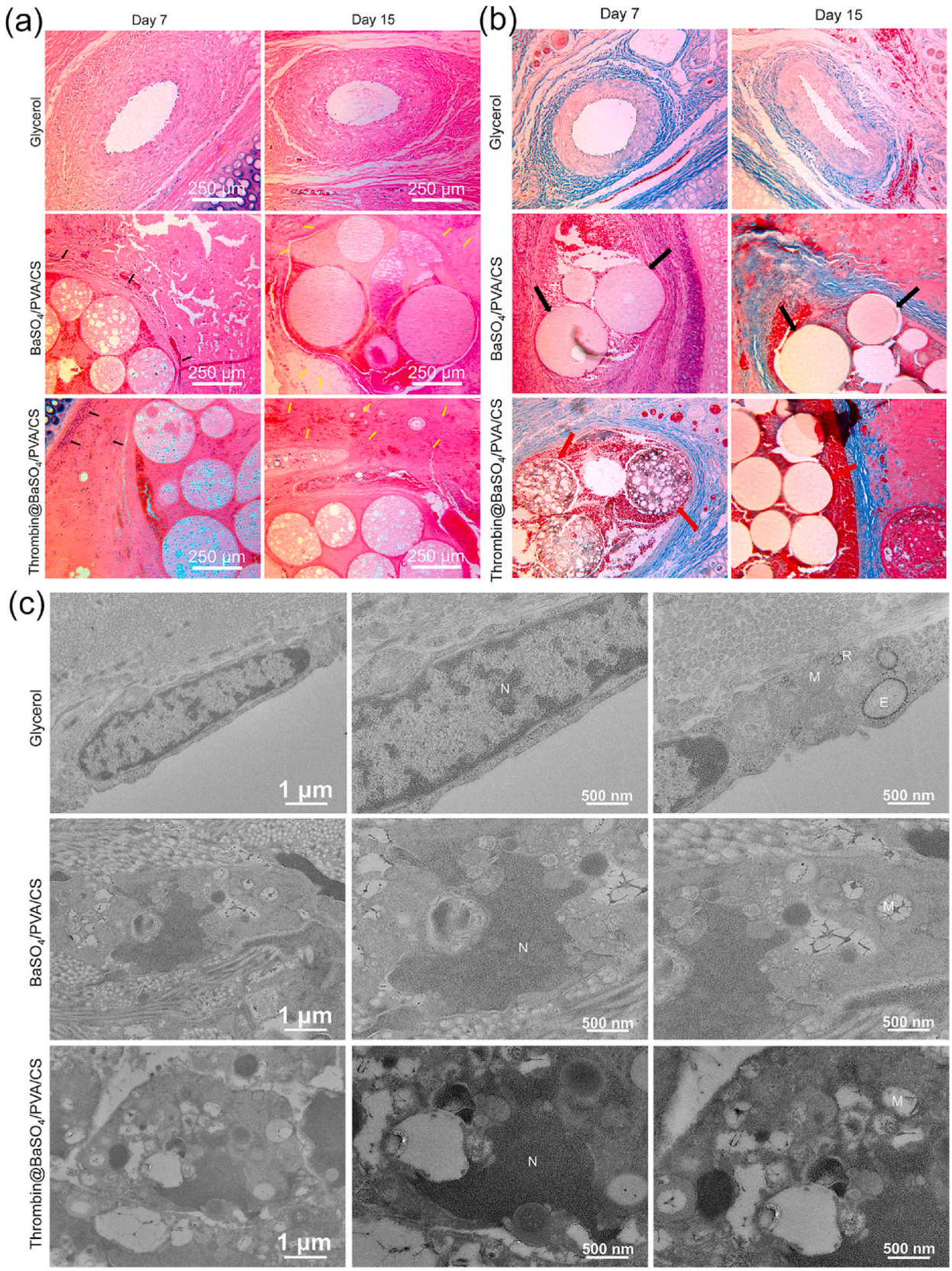

Fig. 8. (a) Macrographs of H&E stained cross-sectional ear arteries treated with glycerol, $BaSO_4$/PVA/CS, and thrombin@$BaSO_4$/PVA/CS MS at different periods (7 and 15 days). Black arrows indicate the inflammatory cells infiltration around the embolized blood vessels, while yellow arrows indicate the diffuse infarction on the periphery of embolized vessels, (b) is the corresponding Masson's trichrome staining images, the black arrows show the $BaSO_4$/PVA/CS MS, while red arrows show the thrombin@$BaSO_4$/PVA/CS MS. (c) FETEM images showing the effects of ischemia induced by the persistent embolization with MS for 15 days, which displays severe degeneration of endothelial cells with extensive ultrastructural changes compared to the glycerol group. [Nucleus (N); Ribosome (R); Endoplasmic reticulum (E); Mitochondria (M)].

15, the ischemic necrosis seemed to be more pronounced as large areas of blackened ear tissue were formed and a definite demarcation became apparent between the damaged and normal tissues. In the present study, we attempted to perform the embolization to an extended period up to 21 days to evaluate the treatment efficacy. Nevertheless, the acute damaged ear tissue became dried and separated from the normal tissue, and the macroscopic appearance of the treated ears could not be taken. The results demonstrate that the developed $BaSO_4$/PVA/CS and thrombin@$BaSO_4$/PVA/CS MS could achieve obvious vascular embolization effects, suggesting their great potential in endovascular embolization treatments of various diseases.

3.6.2. X-ray visibility in vivo

In the clinic, it is desirable to monitor the embolic agents by imaging equipment to allow their precise control and facilitate a convenient post-embolization diagnosis [14,18,59]. The radiopaque $BaSO_4$/PVA/CS MS were assayed for their detectability *in vivo* with fluoroscopy at day 3, day 7, and day 15, respectively. As depicted in Fig. 6b, the PVA/CS MS in the left ear were not visible under the X-ray, whereas the ear artery treated with $BaSO_4$/PVA/CS MS showed clear radiopacity, which was derived from the $BaSO_4$ NPs loaded in the MS. More importantly, it is evident that the radiopacity of MS persisted for the duration of 7 and 15 days, without a reduction in visibility. These results demonstrate that the $BaSO_4$/PVA/CS MS could be detected by fluoroscopy *in vivo* and the X-ray detectability could be maintained for at least 15 days.

3.7. Histopathological and ultrastructural analysis

3.7.1. Histopathological analysis

To further determine the embolization efficacy of $BaSO_4$/PVA/CS and thrombin@$BaSO_4$/PVA/CS MS, the histopathological examinations were performed *via* H&E staining at 7 and 15 days post-embolization. Fig. 8a shows the histological features of the cross-sections of rabbit ear tissues with different treatments. Microscopically, the morphology of ear arteries embolized with glycerol exhibited empty in the vascular lumen and did not show pathological changes after embolization for 7 and 15 days. It was speculated that the glycerol had spread away with the blood into the distal branch arteries and, thus, no evidence of tissue damage or inflammatory reactions was observed around the ear arteries. In contrast, the auricular embolization with free and thrombin-immobilized $BaSO_4$/PVA/CS MS showed that a few individual MS were integrated within the ear arteries, and encapsulated within the coagulative thrombus to lead to mechanical vascular occlusion after embolization for 7 days. A mild foreign body reaction with neutrophils and lymphocytes infiltration was found to be provoked around the embolized MS (black arrows), which is in accordance with the histological findings in previous studies [60,61]. After 15 days, the embolic MS were still retained in the embolized arteries and the inflammatory response was eliminated. It should be noted that the ear parenchyma showed large areas of diffuse infarction on the periphery of embolized ears (indicated by yellow arrows), which accounted for the persistent vascular occlusion by the MS. The results of the histology examination coincide well with the macroscopic observations (Fig. 7a).

As extended *in vivo* embolization could result in infarct evolution and deposition of the collagenous matrix surrounding the embolized arteries, the Masson's trichrome staining was performed to evaluate the necrotic changes after treatments with the embolic materials. As displayed in Fig. 8b, the histopathological assessment of the glycerol injection group carried out for 7 and 15 days revealed no evidence of foreign body reaction or collagen deposition in the ear parenchyma. Compared to the control group, the Masson's trichrome-stained sections in the $BaSO_4$/PVA/CS MS group showed that the visible regions of mild fibrotic tissue could be distinguished from the infarct border zone with collagen bundles formation, which correlated with the thrombin@-$BaSO_4$/PVA/CS MS group after embolization for 7 days. After 15 days, there were extensive infarcts with abundant interstitial fibrosis in the perivascular tissues, which could be due to the persistent occlusion of the ear-feeding arteries and induced ischemia. The progressive fibrosis formation further confirms that the $BaSO_4$/PVA/CS and thrombin@-$BaSO_4$/PVA/CS MS prepared in this study could obstruct the blood and achieve effective artery occlusion.

3.7.2. Ultrastructural changes

The ultrastructural changes in the nucleus and cytoplasm of endothelial cells in the rabbit ear arteries, treated with glycerol and MS for 15 days, were investigated *via* FETEM. As illustrated in Fig. 8c, in the glycerol group (control), the endothelial cells preserved their integrity and normal appearance of the intracellular structures, where the cytoplasmic organelles including mitochondria, ribosome, and endoplasmic reticulum were well developed without structural changes. Conversely, in the $BaSO_4$/PVA/CS and thrombin@$BaSO_4$/PVA/CS MS groups, the endothelial cells experienced severe degeneration with structural variations as compared to the control group. The FETEM observations showed that the nucleus was degenerated with a pleomorphic shape and an indistinct nuclear membrane. In addition, a severely condensed and unevenly distributed chromatin was observed. Moreover, the prominent changes in the cytoplasm were also discerned, which included mitochondria swelling, depletion of the ribosome and endoplasmic reticulum, and cytoplasmic vacuolations. These results are consistent with the previous studies [62–64]. Altogether, the thorough disintegrative necrosis of nucleus and cytoplasm could be due to the endothelial cell damage caused by the persistent MS embolization, which would result in dysfunction of blood perfusion and continued hypoxia due to the alternations in endothelial permeability [65].

4. Conclusions

In this work, the X-ray radiopaque $BaSO_4$@PVA/CS MS were successfully prepared *via* S/W/O emulsification crosslinking method, where $BaSO_4$ NPs were first synthesized as imaging contrast agents, and then mixed with the PVA/CS polymeric matrix. The sieved MS were spherical in shape with desirable particle size ranging from 100 to 300 μm. *In vitro* cytocompatiblity and hemocompatibility tests demonstrated the non-cytotoxic nature and permissible hemolysis rate of the prepared MS. Importantly, *in vitro* and *in vivo* evaluations revealed that the MS were clearly visible on X-ray fluoroscopy by virtue of the loaded $BaSO_4$ NPs. The surface modification with thrombin endowed the MS with excellent hemostatic activities. The results indicated that the thrombin@$BaSO_4$/PVA/CS MS could promote a rapid thrombus formation, as well as facilitate whole blood coagulation, RBCs adhesion, and fibrin generation. Moreover, *in vivo* embolization in a rabbit ear model indicated that both the $BaSO_4$/PVA/CS and thrombin@$BaSO_4$/PVA/CS MS could lead to progressive ischemic necrosis on ears as a result of the effective vascular occlusion. Furthermore, the embolization effect also resulted in abnormal changes of endothelial cells in the embolized rabbit ears. Taken together, the thrombin@$BaSO_4$/PVA/CS MS provide the basis for precise embolization and localized coagulation stimulation, which would enhance the embolization efficiency for various applications.

CRediT authorship contribution statement

Xiaohong Li: Conceptualization, Methodology, Data curation, Writing - original draft. **Xiongfa Ji:** Methodology, Data curation, Investigation. **Kun Chen:** Software, Formal analysis. **Muhammad Wajid Ullah:** Writing - review & editing, Data curation. **Basen Li:** Methodology, Data curation, Resources. **Jiameng Cao:** Formal analysis, Investigation. **Lin Xiao:** Data curation, Validation, Software, Writing - review & editing. **Jun Xiao:** Conceptualization, Resources, Methodology, Data curation. **Guang Yang:** Supervision, Conceptualization, Writing - review & editing, Funding acquisition.

Declaration of competing interest

The authors have no conflicts of interest to declare.

Acknowledgements

This work was financially supported by the National Natural Science Foundation of China (51803067, 21774039, 51973076), and National Key Research and Development Program of China (2018YFE0123700). We extend our sincere appreciation to the Analysis and Test Center of Huazhong University of Science and Technology for the related characterizations, analysis, and measurements.

Appendix A. Supplementary data

Supplementary data to this article can be found online at https://doi.org/10.1016/j.bioactmat.2020.12.013.

References

[1] M. Bai, T. Pan, C. Zhou, M. Li, J. Chen, Z. Zeng, D. Zhu, C. Wu, Z. Jiang, Z. Li, M. Huang, Transarterial chemoembolization with pirarubicin-eluting microspheres in patients with unresectable hepatocellular carcinoma: preliminary results, J. Intev. Med. 2 (2) (2019) 69–77.

[2] R. Ayyagari, T. Powell, L. Staib, J. Chapiro, A. Raja, S. Bhatia, T. Chai, S. Schoenberger, R. Devito, Prostatic artery embolization using 100-300 μm trisacryl gelatin microspheres to treat lower urinary tract symptoms attributable to benign prostatic hyperplasia: a single-center outcomes analysis with medium-term follow-up, J. Vasc. Intervent. Radiol. 31 (1) (2020) 99–107.

[3] K. Fischer, N.J. McDannold, C.M. Tempany, F.A. Jolesz, F.M. Fennessy, Potential of minimally invasive procedures in the treatment of uterine fibroids: a focus on magnetic resonance-guided focused ultrasound therapy, Int. J. Womens Health 7 (2015) 901–912.

[4] Z.X. Shi, J. Yang, H.W. Liang, Z.H. Cai, B. Bai, Emergency transcatheter arterial embolization for massive gastrointestinal arterial hemorrhage, Medicine 96 (52) (2017) e9437.

[5] M. Caine, D. Carugo, X. Zhang, M. Hill, M.R. Dreher, A.L. Lewis, Review of the development of methods for characterization of microspheres for use in embolotherapy: translating bench to cathlab, Adv. Healthc. Mater. 6 (9) (2017).

[6] A. Poursaid, M.M. Jensen, E. Huo, H. Ghandehari, Polymeric materials for embolic and chemoembolic applications, J. Control Release 240 (2016) 414–433.

[7] L. Tian, L. Lu, J. Feng, M.P. Melancon, Radiopaque nano and polymeric materials for atherosclerosis imaging, embolization and other catheterization procedures, Acta Pharm. Sin. B 8 (3) (2018) 360–370.

[8] R. Duran, K. Sharma, M.R. Dreher, K. Ashrafi, S. Mirpour, M. De Lin, R. E. Schernthaner, T.R. Schlachter, V. Tacher, A.L. Lewis, S. Willis, M. Den Hartog, A. Radaelli, A.H. Negussie, B.J. Wood, J.F.H. Geschwind, A novel inherently radiopaque bead for transarterial embolization to treat liver cancer - a pre-clinical study, Theranostics 6 (1) (2016) 28–39.

[9] D. Torres, N.V. Costa, J. Pisco, L.C. Pinheiro, A.G. Oliveira, T. Bilhim, Prostatic artery embolization for benign prostatic hyperplasia: prospective randomized trial of 100-300 μm versus 300-500 μm versus 100- to 300-μm + 300- to 500-μm Embospheres, J. Vasc. Intervent. Radiol. 30 (5) (2019) 638–644.

[10] L. Du, Y. Huang, Q. Zhang, Y. Zhou, J. Huang, L. Yan, Z. Yu, A. Qin, H. Yang, M. Chen, L. Liang, B. Bian, X. Li, J. Fu, Synthesis and assessment of drug-eluting microspheres for transcatheter arterial chemoembolization, Acta Biomater. 88 (2019) 370–382.

[11] M. Caine, T. Chung, H. Kilpatrick, Z. Bascal, S. Willis, Y. Tang, T. de Baere, M. Dreher, A. Lewis, Evaluation of novel formulations for transarterial chemoembolization: combining elements of lipiodol emulsions with drug-eluting beads, Theranostics 9 (19) (2019) 5626–5641.

[12] L.E. Cole, R.D. Ross, J.M. Tilley, T. Vargogogola, R.K. Roeder, Gold nanoparticles as contrast agents in x-ray imaging and computed tomography, Nanomedicine 10 (2) (2015) 321–341.

[13] S.Y. Lee, C.M. Rhee, A.M. Leung, L.E. Braverman, G.A. Brent, E.N. Pearce, A review: radiographic iodinated contrast media-induced thyroid dysfunction, J. Clin. Endocrinol. Metab. 100 (2) (2015) 376–383.

[14] K.V. Sharma, Z. Bascal, H. Kilpatrick, K. Ashrafi, S.L. Willis, M.R. Dreher, A. L. Lewis, Long-term biocompatibility, imaging appearance and tissue effects associated with delivery of a novel radiopaque embolization bead for image-guided therapy, Biomaterials 103 (2016) 293–304.

[15] K. Ashrafi, Y. Tang, H. Britton, O. Domenge, D. Blino, A.J. Bushby, K. Shuturminska, M. den Hartog, A. Radaelli, A.H. Negussie, A.S. Mikhail, D. L. Woods, V. Krishnasamy, E.B. Levy, B.J. Wood, S.L. Willis, M.R. Dreher, A. L. Lewis, Characterization of a novel intrinsically radiopaque Drug-eluting Bead for image-guided therapy: DC Bead LUMI^{TM}, J. Control Release 250 (2017) 36–47.

[16] F. Stacul, A.J. Van Der Molen, P. Reimer, J.A.W. Webb, H.S. Thomsen, S.K. Morcos, T. Almén, P. Aspelin, M.F. Bellin, O. Clement, G. Heinz-Peer, Contrast induced nephropathy: updated ESUR contrast media safety committee guidelines, Eur. Radiol. 21 (12) (2011) 2527–2541.

[17] Q. Wang, K. Qian, S. Liu, Y. Yang, B. Liang, C. Zheng, X. Yang, H. Xu, A.Q. Shen, X-ray visible and uniform alginate microspheres loaded with in situ synthesized $BaSO_4$ nanoparticles for in vivo transcatheter arterial embolization, Biomacromolecules 16 (2015) 1240–1246.

[18] J. Zeng, L. Li, H. Zhang, J. Li, L. Liu, G. Zhou, Q. Du, C. Zheng, X. Yang, Radiopaque and uniform alginate microspheres loaded with tantalum nanoparticles for real-time imaging during transcatheter arterial embolization, Theranostics 8 (17) (2018) 4591–4600.

[19] H. Chen, M.M. Rogalski, J.N. Anker, Advances in functional X-ray imaging techniques and contrast agents, Phys. Chem. Chem. Phys. 14 (39) (2012) 13469–13486.

[20] O. Acarturk, M. Lehmicke, H. Aberman, D. Toms, J.O. Hollinger, M. Fulmer, Bone healing response to an injectable calcium phosphate cement with enhanced radiopacity, J. Biomed. Mater. Res. B 86 (1) (2008) 56–62.

[21] P. Mehnati, R. Malekzadeh, M.Y. Sooteh, Application of personal non-lead nano-composite shields for radiation protection in diagnostic radiology: a systematic review and meta-analysis, Nanomedicine J. 7 (3) (2020) 170–182.

[22] R. Gillani, B. Ercan, A. Qiao, T.J. Webster, Nanofunctionalized zirconia and barium sulfate particles as bone cement additives, Int. J. Nanomed. 5 (2010) 1–11.

[23] R. López-Benítez, G.M. Richter, H.U. Kauczor, S. Stampfl, J. Kladeck, B.A. Radeleff, M. Neukamm, P.J. Hallscheidt, Analysis of nontarget embolization mechanisms during embolization and chemoembolization procedures, Cardiovasc. Intervent. Radiol. 32 (4) (2009) 615–622.

[24] H. Ohnishi, S. Miyachi, K. Murao, R. Hiramatsu, K. Takahashi, H. Ohnishi, T. Kuroiwa, Infiltrated embolization of meningioma with dilute cyanoacrylate glue, Neurol. Med-Chir. 57 (1) (2017) 44–50.

[25] R. López-Benítez, B.A. Radeleff, H.M. Barragán-Campos, G. Noeldge, L. Grenacher, G.M. Richter, P. Sauer, M. Büchler, G. Kauffmann, P.J. Hallscheidt, Acute pancreatitis after embolization of liver tumors: frequency and associated risk factors, Pancreatology 7 (1) (2007) 53–62.

[26] B.D. Jagadeesan, M. Grigoryan, A.E. Hassan, A.W. Grande, R.P. Tummala, Endovascular balloon-assisted embolization of intracranial and cervical arteriovenous malformations using dual-lumen coaxial balloon microcatheters and onyx: initial experience, Neurosurgery 73 (2) (2013) 238–243.

[27] E. Lanza, N. Gennaro, D. Poretti, L. Straffi, S. Marcheselli, M. Tramarin, V. Pedicini, Full recovery after non-target cerebral embolization of n-butyl–cyanoacrylate occurred during emergency treatment of a facial arteriovenous malformation, CVIR Endovasc. 2 (2019) 2–6.

[28] L.D. Orozco, G.D. Luzardo, R.F. Buciuc, Transarterial balloon assisted Onyx embolization of pericallosal arteriovenous malformations, J. Neurointerv. Surg. 5 (4) (2013) 1–4.

[29] D.F. Vollherbst, R. Otto, T.D. Do, A. von Deimling, H.U. Kauczor, M. Bendszus, C. M. Sommer, M.A. Möhlenbruch, Extra-small dual-lumen micro-balloon catheters can improve endovascular embolization: an experimental in vivo and in vitro study, J. Neurointerv. Surg. 10 (11) (2018) 1092–1096.

[30] J. Fifi, Y. Niimi, A. Berenstein, Onyx embolization of an extensive mandibular arteriovenous malformation via a dual lumen balloon catheter: a technical case report, J. Neurointerv. Surg. 5 (2) (2013) 5–7.

[31] H. Okada, J. Chung, D.M. Heiferman, D.K. Lopes, Assessment of human placenta as an ex-vivo vascular model for testing of liquid embolic agent injections with adjunctive techniques, J. Neurointerv. Surg. 10 (9) (2018) 892–895.

[32] P. Qi, M.F. Maitz, N. Huang, Surface modification of cardiovascular materials and implants, Surf. Coat Tech. 233 (2013) 80–90.

[33] X. Yang, W. Liu, N. Li, M. Wang, B. Liang, I. Ullah, A. Luis Neve, Y. Feng, H. Chen, C. Shi, Design and development of polysaccharide hemostatic materials and their hemostatic mechanism, Biomater. Sci. 5 (12) (2017) 2357–2368.

[34] M. Teodorescu, M. Bercea, S. Morariu, Biomaterials of poly(vinyl alcohol) and natural polymers, Polym. Rev. 58 (2) (2018) 247–287.

[35] A. Kumar, S.S. Han, PVA-based hydrogels for tissue engineering: a review, Int. J. Polym. Mater. Po. 66 (4) (2017) 159–182.

[36] R.A. Sheth, S. Sabir, S. Krishnamurthy, R.K. Avery, Y.S. Zhang, A. Khademhosseini, R. Oklu, Endovascular embolization by transcatheter delivery of particles: past, present, and future, J. Funct. Biomater. 8 (2) (2017) 12.

[37] S. Qiu, N.J. Ge, D.K. Sun, S. Zhao, J.F. Sun, Z.B. Guo, K. Hu, N. Gu, Synthesis and characterization of magnetic polyvinyl alcohol (PVA) hydrogel microspheres for the embolization of blood vessel, IEEE Trans. Biomed. Eng. 63 (4) (2016) 730–736.

[38] ISO-10993-5: Biological Evaluation of Medical Devices - Part 5: Tests for Cytotoxicity: in Vitro Methods, ANSI/AAMI, Arlington, VA, 1999.

[39] Y. Wang, Y. Fu, J. Li, Y. Mu, X. Zhang, K. Zhang, M. Liang, C. Feng, X. Chen, Multifunctional chitosan/dopamine/diatom-biosilica composite beads for rapid blood coagulation, Carbohydr. Polym. 200 (2018) 6–14.

[40] V.A. Kumar, N.L. Taylor, A.A. Jalan, L.K. Hwang, B.K. Wang, J.D. Hartgerink, A nanostructured synthetic collagen mimic for hemostasis, Biomacromolecules 15 (4) (2014) 1484–1490.

[41] E.Y. Chung, H.M. Kim, G.H. Lee, B.K. Kwak, J.S. Jung, H.J. Kuh, J. Lee, Design of deformable chitosan microspheres loaded with superparamagnetic iron oxide nanoparticles for embolotherapy detectable by magnetic resonance imaging, Carbohydr. Polym. 90 (4) (2012) 1725–1731.

[42] Z. Li, M. Kawashita, T.A. Kudo, H. Kanetaka, Sol–gel synthesis, characterization, and in vitro compatibility of iron nanoparticle-encapsulating silica microspheres for hyperthermia in cancer therapy, J. Mater. Sci. Mater. Med. 23 (2012) 2461–2469.

[43] X. Sun, H. Dai, P. Guo, X. Sha, Biocompatibility of a new kind of polyvinyl alcohol embolic microspheres: in vitro and in vivo evaluation, Mol. Biotechnol. 61 (8) (2019) 610–621.

[44] S. Gao, Z. Yuan, W. Guo, M. Chen, S. Liu, T. Xi, Q. Guo, Comparison of glutaraldehyde and carbodiimides to crosslink tissue engineering scaffolds fabricated by decellularized porcine menisci, Mat. Sci. Eng. C-Mater. 71 (2017) 891–900.
[45] G. Ghafourifar, K.C. Waldron, Capillary electrophoretic peptide mapping to probe the immobilization/digestion conditions of glutaraldehyde-crosslinked chymotrypsin, Curr. Anal. Chem. 12 (9) (2016) 65–73.
[46] A. Monnier, C. Rombouts, D. Kouider, I. About, H. Fessi, N. Sheibat-Othman, Preparation and characterization of biodegradable polyhydroxybutyrate-co-hydroxyvalerate/polyethylene glycol-based microspheres, Int. J. Pharm. 513 (1–2) (2016) 49–61.
[47] W. Zeng, J. Huang, X. Hu, W. Xiao, M. Rong, Z. Yuan, Z. Luo, Ionically cross-linked chitosan microspheres for controlled release of bioactive nerve growth factor, Int. J. Pharm. 421 (2) (2011) 283–290.
[48] X. Zhou, M. Kong, X. Cheng, J. Li, J. Li, X. Chen, Investigation of acetylated chitosan microspheres as potential chemoembolic agents, Colloid Surface B 123 (2014) 387–394.
[49] Y. Yildiz-Peköz, O. Akbal, S.H. Tekarslan, A.O. Sagirli, L. Mulazimoglu, D. Morina, E. Cevher, Preparation and characterization of doripenem-loaded microparticles for pulmonary delivery, J. Aerosol. Med. Pulm. D 31 (6) (2018) 1378–1388.
[50] E. Campos, P. Coimbra, M.H. Gil, An improved method for preparing glutaraldehyde cross-linked chitosan-poly(vinyl alcohol) microparticles, Polym. Bull. 70 (2013) 549–561.
[51] G. Sun, C. Feng, C. Jiang, T. Zhang, Z. Bao, Y. Zuo, M. Kong, X. Cheng, Y. Liu, X. Chen, Thermo-responsive hydroxybutyl chitosan hydrogel as artery intervention embolic agent for hemorrhage control, Int. J. Biol. Macromol. 105 (2017) 566–574.
[52] F. Xuan, J. Rong, M. Liang, X. Zhang, J. Sun, L. Zhao, Y. Li, D. Liu, F. Li, X. Wang, Y. Han, Biocompatibility and effectiveness evaluation of a new hemostatic embolization agent: thrombin loaded alginate calcium microsphere, BioMed Res. Int. 2017 (2017).
[53] T. Liu, W. Xue, B. Ke, M. Xie, D. Ma, Star-shaped cyclodextrin-poly($_L$-lysine) derivative co-delivering docetaxel and MMP-9 siRNA plasmid in cancer therapy, Biomaterials 35 (12) (2014) 3865–3872.
[54] P. Huang, Y. Zhao, S. Kuga, M. Wu, Y. Huang, A versatile method for producing functionalized cellulose nanofibers and their application, Nanoscale 8 (6) (2016) 3753–3759.
[55] J. Qian, Y. Chen, H. Yang, C. Zhao, X. Zhao, H. Guo, Preparation and characterization of crosslinked porous starch hemostatic, Int. J. Biol. Macromol. 160 (2020) 429–436.
[56] L.W. Chan, C.H. Kim, X. Wang, S.H. Pun, N.J. White, T.H. Kim, PolySTAT-modified chitosan gauzes for improved hemostasis in external hemorrhage, Acta Biomater. 31 (2016) 178–185.
[57] G. Singh, A. Nayal, S. Malhotra, V. Koul, Dual functionalized chitosan based composite hydrogel for haemostatic efficacy and adhesive property, Carbohydr. Polym. 247 (2020), 116757.
[58] D. Zhu, Mathematical modeling of blood coagulation cascade: kinetics of intrinsic and extrinsic pathways in normal and deficient conditions, Blood Coagul. Fibrin. 18 (7) (2007) 637–646.
[59] Q. Du, L. Li, Y. Liu, J. Zeng, J. Li, C. Zheng, G. Zhou, X. Yang, Fabrication of inherently radiopaque $BaSO_4$@BaAlg microspheres by a one-step electrospraying method for embolization, J. Mater. Chem. B 6 (2018) 3522–3530.
[60] X. Su, L. Bu, H. Dong, S. Fu, R. Zhuo, Z. Zhong, An injectable PEG-based hydrogel synthesized by strain-promoted alkyne-azide cycloaddition for use as an embolic agent, RSC Adv. 6 (4) (2016) 2904–2909.
[61] S. Gupta, K.C. Wright, J. Ensor, C.S. Van Pelt, K.A. Dixon, V. Kundra, Hepatic arterial embolization with doxorubicin-loaded superabsorbent polymer microspheres in a rabbit liver tumor model, Cardiovasc. Intervent. Radiol. 34 (5) (2011) 1021–1030.
[62] H. Jin, S. Li, Ruan Li, Changes of the ultrastructures of pulmonary vascular endothelial cells and the content of nitric oxide in serum after acute pulmonary embolism in rabbits, Acta Anat. Sin. 48 (5) (2017) 565–570.
[63] Y. Iwao, H. Ojima, T. Kobayashi, Y. Kishi, S. Nara, M. Esaki, K. Shimada, N. Hiraoka, M. Tanabe, Y. Kanai, Liver atrophy after percutaneous transhepatic portal embolization occurs in two histological phases: hepatocellular atrophy followed by apoptosis, World J. Hepatol. 9 (32) (2017) 1227–1238.
[64] J.A. Watts, J. Zagorski, M.A. Gellar, B.G. Stevinson, J.A. Kline, Cardiac inflammation contributes to right ventricular dysfunction following experimental pulmonary embolism in rats, J. Mol. Cell. Cardiol. 41 (2006) 296–307.
[65] J.F. Tomashefski, A.M. Cohen, C.F. Doershuk, Longterm histopathologic follow-up of bronchial arteries after therapeutic embolization with polyvinyl alcohol (Ivalon) in patients with cystic fibrosis, Hum. Pathol. 19 (1988) 555–561.